Non-Hermitian Control between Absorption and Transparency in Reflectionless Magnonics

Jie Qian
Fudan University
J.W. Rao
Shanghaitech University https://orcid.org/0000-0002-7199-1302
Zejin Rao
Fudan University
Zhenghua An (anzhenghua@fudan.edu.cn)
Fudan University https://orcid.org/0000-0001-8664-6184
Yongsheng Gui
University of Manitoba
Can-Ming Hu
University of Manitoba https://orcid.org/0000-0002-9838-9848

Article

Keywords:

Posted Date: April 14th, 2022

DOI: https://doi.org/10.21203/rs.3.rs-1476165/v1

Non-Hermitian Control between Absorption and Transparency in Reflectionless Magnonics

Jie Qian[1,2], J.W. Rao[3], Z. J. Rao[1], Zhenghua An[1,4,*], Yongsheng Gui[2] and C. -M. Hu[2,*]

[1] *State Key Laboratory of Surface Physics, Institute of Nanoelectronic Devices and Quantum Computing, Department of Physics, Fudan University, Shanghai 200433, China*
[2] *Department of Physics and Astronomy, University of Manitoba, Winnipeg R3T 2N2, Canada*
[3] *School of Physical Science and Technology, Shanghaitech University, Shanghai 201210, China.*
[4] *Shanghai Qi Zhi Institute, 41th Floor, AI Tower, No. 701 Yunjin Road, Xuhui District, Shanghai, 200232, China*

[*]Email: anzhenghua@fudan.edu.cn
[*]Email: Can-Ming.Hu@umanitoba.ca

Abstract

Photon propagation with controllable absorption/transmission and meanwhile vanishing reflection is highly desired for many practical applications. Recent works in metamaterials and transformation optics have demonstrated promising progresses including coherent perfect absorption/transparency (PA/PT), electromagnetically induced transparency, cloaking or invisibility etc. However, most of these reported works eluded the non-Hermicity nature of the open systems. Meanwhile, reported works in non-Hermitian physics field focused mainly on the eigenstate properties and less attention has been paid to the reflection condition despite that perfect zero-reflection (PZR) is a prerequisite condition to realize actual applications like PA/PT. Here we demonstrate that the coupled system of two subwavelength-sized magnon resonators on a same microwave transmission line exhibits remarkable non-Hermitian properties such as level repulsion (LR) and level attraction (LA) interactions and meanwhile allows the reflection to be tuned to perfect zero. The observed PZR condition is found to exhibit an infinitely narrow bandwidth and meanwhile an infinite discontinuity in the group delay. This singularity in reflection distinguishes from the eigenstates of magnonic polaritons but can be adjusted on or off resonance with the eigenstates. Accordingly, the absorption and transmission can be flexibly tuned

from nearly PA to nearly PT regimes. Our work not only enriches non-Hermitian physics in magnon-photon coupled systems but also brings important implications to practical applications such as microwave circuits, photonic chips and quantum information.

Introduction

Manipulating photon transmission/absorption in a predesigned manner while keeping zero reflection is important for many practical applications in general wave optics. For real applications, the transmitted photons are critical not only for signal transfer and/or filtering, but also can reveal important light-matter interaction physics[1] (such as in electromagnetically induced transparency[2]) and may be encoded for information processing. The absorbed photons are crucial for signal conversion (e.g., photoelectric detection[3-7]) and energy harvesting[8] (e.g. photothermal, photoelectric, photo-spin-voltaic[9] or photomagnonic[10] conversions). The reflected photons, however, are often harmful not only because the transmission/absorption efficiency can be sacrificed, but also reflected photons can interfere with excitation and then play detrimental effects to the performance of whole optical setup (e.g., the frequency stability of the excitation laser)[11]. It is therefore highly anticipated to maintain a vanishing reflection and then tailor transmission/absorption for specific applications[12-14].

To this aim, tremendous efforts have been made in several closely related fields. In metamaterials, significant progresses such as perfect absorption/transparency (PA/PT)[15-17] and electromagnetically induced transparency/absorption (EIT/EIA)[18-21] have been reported. Transformation optics has demonstrated cloaking and provided us a strategy for finding zero reflection condition with inhomogeneous, anisotropic materials (i.e., transformation media). Optical systems with parity-time symmetry attract increasing interest partly because they can suppress reflection[22]. Horsley *et al* introduced Kramers-Kronig complex potentials which can approach reflectionless propagation of photons[23]. In most of these works, however, the non-Hermicity nature of the reported open systems was implicit and it remained unclear whether the reflection was sufficiently reduced to perfect zero or not. On the other hand, in non-Hermitian physics, very recent works focused mainly on the singular properties like zero-damping states[24, 25], exceptional points[26, 27], skin effects[28] and so on. Little attention has been paid to the reflection

spectra despite that perfect zero-reflection (PZR) is a prerequisite condition to realize anticipated applications like PA/PT.

Here, we propose a magnonic device with two low-damping yttrium iron garnet (YIG) spheres coupled to a same microwave transmission line (MTL). These two magnonic resonators can exchange photons with the common environment (i.e., MTL) and couple indirectly to each other, mediated by the travelling wave along MTL. Utilizing the non-hermitian property by adjusting the retardation phase (Φ) between two magnonic resonators, we can control the hybridization states from level repulsion (LR) to level attraction (LA) regimes. We explicitly show that, in the complex frequency plane, the zero reflection (ZR) condition is not identical to the resonant eigenstates in our two-port configuration, unlike in one-port configuration where ZR coincides with the resonant eigenstates making PA achievable. By tuning the ZR condition on or off resonance with the eigenstate, we can control the absorption/transparency in a coherent manner. Nearly PA and PT can hence be realized and flexible tuning inbetween therefore becomes applicable. Our work expands the non-Hermitian physics in magnon-photon coupled systems and sheds light to the practical applications such as microwave circuits, photonic chips and quantum information.

Results

Structure of coherent magnonic system. In our device (Fig. 1a) two 1-mm diameter yttrium iron garnet (YIG 1 and YIG 2) spheres are placed above a transmission line (MTL) with a mutual distance of $l = 25\,mm$. Microwave is input from either port 1 or port 2 to excite two magnonic oscillators. An external magnetic field (H-field) is applied perpendicularly to the planar, which saturates the magnetization of two YIG spheres and determines the ferromagnetic resonant frequency of two magnon modes (ω_1 and ω_2). To fine tune their frequency detuning $\Delta_H \equiv \omega_1 - \omega_2$, an additional small coil is embedded under YIG 1 so that its local magnetic field (δH) can be precisely adjusted via coil current. As a result, two nonidentical resonators with excellent tunability in resonant frequencies (ω_1 is determined by $H + \delta H$ and ω_2, by H) are configured. In addition, the frequency detuning Δ_H can be finely adjusted with a very high accuracy better than the intrinsic/extrinsic damping rates (due to δH). Such a tunability with a good accuracy

makes our configuration be unique and superior for studying photon-mediated coupled-resonance since the resonance wavelengths in most previously works are fixed, e.g., atomic systems[29,30].

As schematically shown in Fig. 1b, the excited resonators (YIG 1 and YIG 2) can relax their energy either through intrinsic damping ($\gamma_{1,2}$) or by exchanging energy with the common environment (MTL). The intrinsic damping rates ($\gamma_{1,2}$) are typically low and depend on the natural properties of YIG spheres including the surface roughness, impurities and defects etc. The energy dissipation into the common MTL are characterized by the extrinsic/radiative damping rates $\kappa_{1,2}$. Taking account of the coherent propagation of microwave photons in between two resonators, two resonators are correlated with the coupling strength of $i\Gamma e^{i\Phi}$, in which $\Gamma = \sqrt{\kappa_1\kappa_2}$ due to the correlation between κ_1 and κ_2, and Φ is the microwave propagation phase and it depends apparently on the distance (l) between two resonators, $\Phi = kl$ (k is the wave number of microwave in MTL). Since here l is large enough to suppress the direct coupling between two resonators, the above indirect coupling mediated with coherent photons dominates the system properties. Depending on the value of Φ, the coupling between two YIG resonators can be either purely real or purely imaginary, or mixed real and imaginary contributions: the real part contributes to coherent coupling, while the imaginary part contributes to dissipative coupling. In order to tune the interaction via Φ, either the wave number (k) or the distance (l) can be adjusted and, in our experiment, we choose to change k at a fixed distance l because relocation of the YIGs' position requiring a very high mechanical accuracy, may not only change l, but also affect other important parameters like $\kappa_{1,2}$. When the external magnetic field H is swept over a large range, the resonant frequencies and thereby k are modulated accordingly. (Note that the influence of local field to k can be neglected, since $\delta H \ll H$ and hence $\Delta_H \ll \omega_{1,2}$). Such a non-mechanical method to tune the effective length in terms of resonant wavelength is highly favored for both exploration of exotic non-hermitian physics and for real applications[30]. As a result, Φ offers a large freedom to tune the non-Hermitian properties of the coupled system and hence the reflection/transmission properties, as will be seen later.

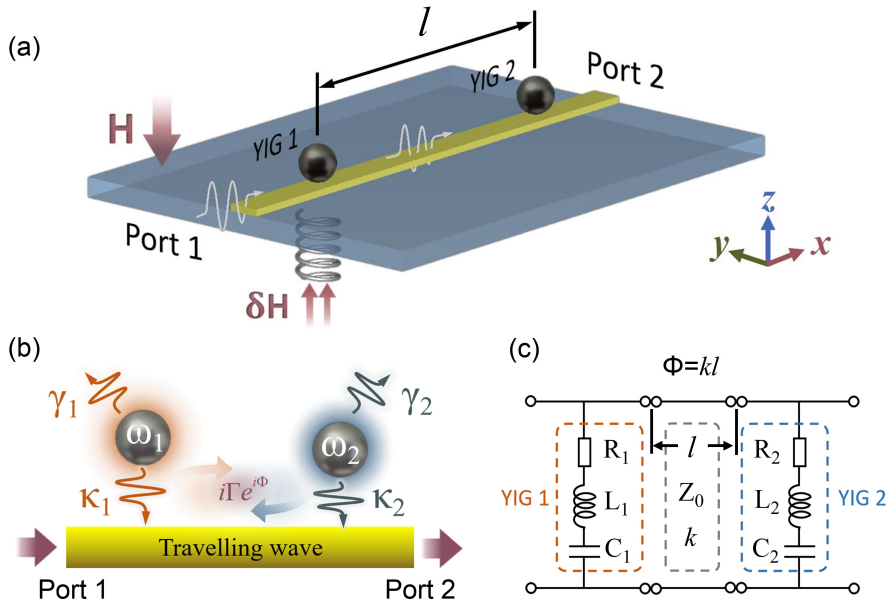

Fig. 1 Coherent magnonic system. a Schematic diagram of the experimental setup. Two separated magnons ($l = 25\,mm$) coupled to a transmission line are placed under a vertical magnetic field ($H-$ field), the local magnetic field ($H + \delta H$) around YIG 1 is controllable independently by finely-adjusting coil current. **b** Schematic diagram showing two resonators are side-coupled with a transmission line and interact with each other mediated by travelling wave with the coupling strength of $i\Gamma e^{i\Phi}$. **c** Equivalent circuit of the coupled system. Circuit elements used to model the two YIG spheres are highlighted by the orange and blue box, respectively.

Non-Hermiticity of the coupled system. We start with the coupling characteristics of the system. When mode frequency detuning Δ_H is small, two magnon modes can be approximately regarded as two linearly coupled harmonic oscillators. Then, taking account of the mutual indirect coupling off-diagonal term $i\Gamma e^{i\Phi}$, the coupled system can be described with a non-Hermitian Hamiltonian,

$$\mathcal{H} = \hbar\tilde{\omega}_1\hat{a}^\dagger\hat{a} + \hbar\tilde{\omega}_2\hat{b}^\dagger\hat{b} + \hbar(i\Gamma e^{i\Phi})(\hat{a}^\dagger\hat{b} + \hat{b}^\dagger\hat{a}) \qquad (1)$$

where $\hat{a}^\dagger$ ($\hat{a}$) and $\hat{b}^\dagger$ ($\hat{b}$) represent the creation (annihilation) operators of the two magnon resonators, obeying the commute relations of $[\hat{a}, \hat{a}^\dagger] = 1$, $[\hat{b}, \hat{b}^\dagger] = 1$ and $[\hat{a}, \hat{b}] = 0$. $\tilde{\omega}_{1,2} = \omega_{1,2} - i(\gamma_{1,2} + \kappa_{1,2})$ are the complex eigenvalues for uncoupled resonators, with the imaginary parts being related to the experimentally observed frequency linewidth. Compared with previous works, Eq.(1) represents a more generalized form which include the Fabry-Pérot type ($\omega_1 = \omega_2, \Phi \neq 0$)[31] and Friedrich-Wintgen type ($\omega_1 \neq \omega_2, \Phi = 0$)[32] interactions and arbitrary Φ values

(not just $\Phi = 0, \pi$[24,25]), except that direct coupling (Hermitian contribution) is ruled out in order to highlight the excellent tunability of the non-hermitian property through travelling coherent photons (Φ).

The eigenvalues of Eq. (1) can be solved to be,

$$\tilde{\omega}_{\pm} = \frac{1}{2}\left[\tilde{\omega}_1 + \tilde{\omega}_2 \pm \sqrt{(\tilde{\omega}_1 - \tilde{\omega}_2)^2 + 4(i\Gamma e^{i\Phi})^2}\right] \qquad (2)$$

where the real parts of $\tilde{\omega}_{\pm}$ give the dispersions of two hybridized modes, and the imaginary parts $\mathrm{Im}(\tilde{\omega}_{\pm})$ correspond to their damping rates. Unlike previous works in which coherent and dissipative couplings are independent[34,35], full range of Φ here allows the system to be continuously tuned from pure dissipative coupling ($\Phi = n\pi$) to pure coherent coupling regimes ($\Phi = (n + 1/2)\pi$). This large tunable freedom makes the present magnonic system a fertile ground for studying non-Hermitian physics and tailor absorption/transparency for specific applications. As an example, in the limit of zero damping ($\gamma_{1,2} \simeq 0$), one eigenmode becomes lossless with a purely real eigenfrequency for $\Phi = n\pi$, approaching Fabry–Pérot type bound state in continuum (BIC)[33] for identical resonators ($\omega_1 = \omega_2$). Also, the square-root singularity can show up at the exceptional point (EP) where two eigenvalues in Eq. (2) will coalesce. In present system with $\gamma_1 \cong \gamma_2$, EPs will appear at the frequency detuning satisfying $\Delta_{\mathrm{H}} = \pm\sqrt{6\kappa_1\kappa_2 - \kappa_1^2 - \kappa_2^2}$ when $3 - 2\sqrt{2} \leq \kappa_1/\kappa_2 \leq 3 + 2\sqrt{2}$ and $\sin\Phi = \pm(\kappa_2 - \kappa_1)/2\sqrt{\kappa_1\kappa_2}$.

To track the variation of eigenstates ($\tilde{\omega}_{\pm}$) with Δ_H in our experiments, we keep ω_2 fixed and scan ω_1 (by finely adjusting δH). Blue lines in Figs. 2a-d plot the real part, $\Delta\mathrm{Re}(\tilde{\omega}_{\pm}) = \mathrm{Re}(\tilde{\omega}_{\pm}) - \omega_2$ as a function of Δ_H in four representative cases, $\Phi = n\pi, (n + 1/4)\pi, (n + 1/2)\pi, (n + 3/4)\pi$, respectively. Realistic parameter values ($\gamma_1/2\pi = \gamma_2/2\pi = 1\mathrm{MHz}$, $\kappa_1/2\pi = 1.7$ MHz, $\kappa_2/2\pi = 3.3$ MHz) are taken to be comparable with later experiment results. Blue lines in Figs. 2e-h depict the corresponding imaginary parts, $\mathrm{Im}(\tilde{\omega}_{\pm})$. For $\Phi = n\pi$, the coupling strength $i\Gamma e^{i\Phi}$ becomes pure imaginary, which indicates only the dissipative coupling effect existing between two magnon modes. As a result, level attraction (LA) occurs: hybridized modes $\Delta\mathrm{Re}(\tilde{\omega}_{\pm})$ attract (Fig. 2a) while the damping rates $\mathrm{Im}(\tilde{\omega}_{\pm})$ repulse each other (FIG. 2e). For $\Phi = (n + 1/2)\pi$, $i\Gamma e^{i\Phi}$ becomes pure real, thus the coupling effect is pure coherent and results in level repulsion (LR) with the distinct features: hybridized modes $\Delta\mathrm{Re}(\tilde{\omega}_{\pm})$ repulse (FIG. 2c) while the damping rates $\mathrm{Im}(\tilde{\omega}_{\pm})$ attract each other (FIG. 2g). Obviously, Φ determines the

complex coupling strength and can control system in which state, LA or LR. When $\Phi = (n + 1/4)\pi$ and $(n + 3/4)\pi$, the indirect coupling strength contributes both coherent (real part) and dissipative (imaginary part) coupling terms, which leads to compromised repulsed modes $\Delta\mathrm{Re}(\tilde{\omega}_{\pm})$ and the damping rate of one hybridized mode can be compensated by the other. For $\Phi = (n + 1/4)\pi$, shadowed blue region in Fig. 2f shows $\mathrm{Im}\,(\tilde{\omega}_{-})/2\pi < \gamma_1 + \gamma_2 = 2$ MHz, which implies the intrinsic damping of mode $\tilde{\omega}_{-}$ is less than the total original intrinsic damping of the uncoupled magnons, owing to the interference of coherent and dissipative coupling and thereby induced energy compensation. Similarly, for $\Phi = (n + 3/4)\pi$ (blue region in Fig. 2h), $\mathrm{Im}\,(\tilde{\omega}_{+})/2\pi < \gamma_1 + \gamma_2 = 2$ MHz. Experimentally, as Φ is controlled by adjusting the wave number of two YIG spheres ($\omega_{1,2}$ or H), we take $\Phi = 1.07\pi, 1.25\pi, 1.37\pi$ ($\mu_0 H = 1160$ Gs, 1380 Gs, 1524 Gs and $\omega_2/2\pi = 3.6$ GHz, 4.24 GHz, 4.69 GHz, respectively) to be three representative conditions. The measured absorption spectral results (see Supplementary Note 3, Figs. S2 (g-i)) clearly identify the above LA and LR states with $\Phi = 1.07\pi$ (LA), 1.25π (LR) and 1.37π (LR), respectively and agree excellently with the theoretical prediction.

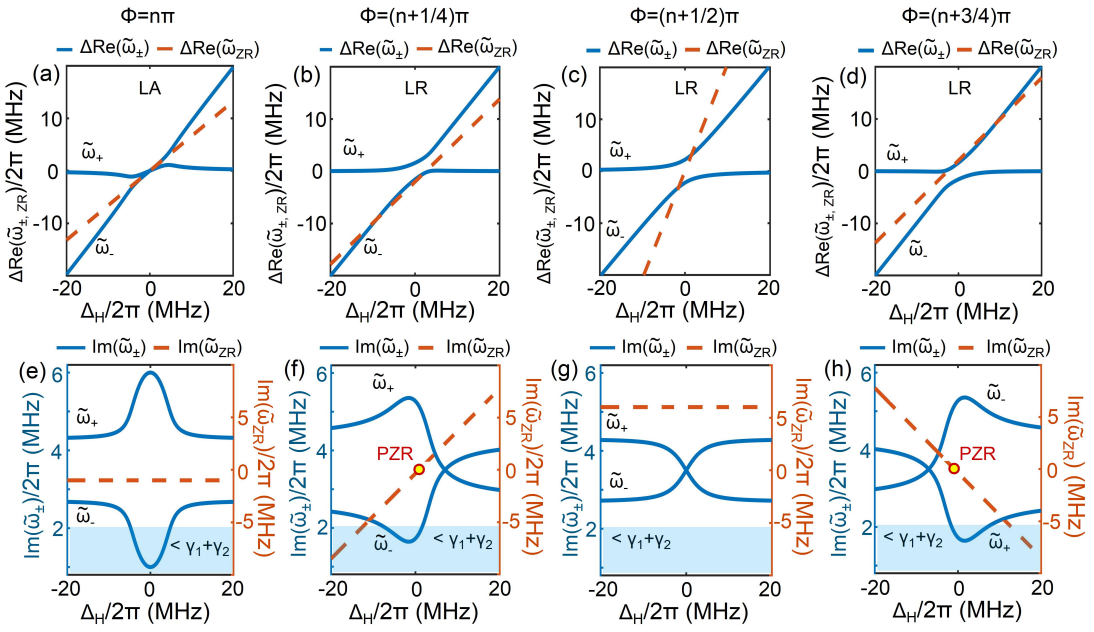

Fig. 2 The evolution between level attraction and level repulsion. a-d blue lines: the frequencies detuning of real parts of eigenvalues $\Delta\mathrm{Re}(\tilde{\omega}_{\pm}) = \mathrm{Re}(\tilde{\omega}_{\pm}) - \omega_2$, orange dashed lines: the frequencies detuning of real part of ZR condition $\Delta\mathrm{Re}(\tilde{\omega}_{ZR}) = \mathrm{Re}(\tilde{\omega}_{ZR}) - \omega_2$ as a function of Δ_H in four Φ cases ($\Phi = n\pi, (n + 1/4)\pi, (n + 1/2)\pi, (n + 3/4)\pi, n \in N^*$). **e-f**

Correspondingly, blue lines: the frequencies detuning of the imaginary parts of eigenvalues $\mathrm{Im}(\tilde{\omega}_{\pm})$, orange dashed lines: the imaginary part of ZR condition $\mathrm{Im}(\tilde{\omega}_{ZR})$ as a function of Δ_H. In which blue lines for $\mathrm{Im}(\tilde{\omega}_{\pm})$ correspond to the left *y*-axis and orange dashed lines $\mathrm{Im}(\tilde{\omega}_{ZR})$ correspond to the right *y*-axis.

Zero-Reflection (ZR) and Perfect Zero-Reflection (PZR) conditions. To analyze the reflection/transmission spectral properties, we find that a classical RLC circuit model is adequate to describe the photon-mediated coupled system (Supplementary Note 1). Fig. 1c shows the equivalent circuit in which two resonant circuits with their own resistance ($R_{1,2}$), inductance ($L_{1,2}$), and capacitance ($C_{1,2}$) are connected in series. The series circuits are highlighted by the orange and blue box, which represent YIG 1 and YIG 2, respectively. Two resonators can thereby be characterized by their resonant frequencies ($\omega_{1,2} = 1/\sqrt{L_{1,2}C_{1,2}}$), their intrinsic ($\gamma_{1,2} = R_{1,2}/2L_{1,2}$) and extrinsic ($\kappa_{1,2} = Z_0/4L_{1,2}$) damping, the subscript 1, 2 corresponds to YIG 1 and YIG 2, respectively. Two resonant circuits are connected in parallel, and $Z_0 = 50\ \Omega$ is the characteristic impedance of the transmission line. The analytical formula for reflection $S_{11}(\omega)$ and transmission $S_{21}(\omega)$ spectra are derived from ABCD matrix[36] method (see details in Supplementary Note 1):

$$S_{11}(\omega) = -2i\omega\frac{\kappa_2 e^{2i\Phi}(X_1 - 2i\omega\kappa_1) + \kappa_1(X_2 + 2i\omega\kappa_2)}{(X_1 + 2i\omega\kappa_1)(X_2 + 2i\omega\kappa_2) + 4\omega^2\kappa_1\kappa_2 e^{2i\Phi}} \quad (3)$$

$$S_{21}(\omega) = \frac{X_1 X_2 e^{i\Phi}}{(X_1 + 2i\omega\kappa_1)(X_2 + 2i\omega\kappa_2) + 4\omega^2\kappa_1\kappa_2 e^{2i\Phi}} \quad (4)$$

where $X_1 = \omega^2 - \omega_1^2 + 2i\omega\gamma_1$, $X_2 = \omega^2 - \omega_2^2 + 2i\omega\gamma_2$. Note that the eigenstates in Eq. (2) correspond to zero denominator in Eqs. (3) and (4) or divergent S_{11} and S_{21}. This agrees neither with ZR ($S_{11} \equiv 0$) nor with zero transmission (ZT, i.e., $S_{21} \equiv 0$) which are required conditions for PA. However, as stated before, ZR is crucially important to enable PA and PT and to avoid harmful interference from the actual application point of view. Considering the non-Hermicity, the solutions of ZR, $S_{11}(\omega) \equiv 0$, in complex frequency plane (Supplementary Note 2) are plotted as orange dashed lines in Fig. 2, in which real parts $\mathrm{Re}(\tilde{\omega}_{ZR})$ are shown in Figs. 2a-d and imaginary parts $\mathrm{Im}(\tilde{\omega}_{ZR})$ are shown in Figs. 2e-h as functions of Δ_H, respectively, for different Φ cases. From Fig. 2, although $\mathrm{Re}(\tilde{\omega}_{ZR})$ depends always on Δ_H with a positive slope, $\mathrm{Im}(\tilde{\omega}_{ZR})$ approaches two constant values (one positive and one negative) at two conditions: when $\Phi = n\pi$,

$\mathrm{Im}(\tilde{\omega}_{ZR}) = -i\frac{\gamma_1\kappa_2+\gamma_2\kappa_1}{\kappa_1+\kappa_2} = -i$ MHz (Fig. 2e, right scale) and when $\Phi = (\mathrm{n}+1/2)\pi$, $\mathrm{Im}(\tilde{\omega}_{ZR}) = i\frac{\gamma_1\kappa_2-\gamma_2\kappa_1-2\kappa_1\kappa_2}{\kappa_1-\kappa_2} = 6i$ MHz (Fig. 2g, right scale). For other Φ values ($\Phi \notin \mathrm{n}\pi, (\mathrm{n}+1/2)\pi$), $\mathrm{Im}(\tilde{\omega}_{ZR})$ becomes dependent on Δ_H and, more importantly, a critical value of $\mathrm{Im}(\tilde{\omega}_{ZR}) = 0$ can be found. This is reminiscent of the zero-damping state in Ref. 24, 25 and an unconventional bound state in the continuum (BIC) in Ref. 26 but both observed only in the transmission spectra. Different from these cavity magnonics system with unbalanced damping rates (e.g., $\kappa_{\mathrm{Cavity}} > \gamma_{\mathrm{Cavity}} > \gamma_{\mathrm{YIG}} > \kappa_{\mathrm{YIG}}$ in Ref. [25]), our system taking advantage of the low and balanced radiative damping feature of pure magnons ($\gamma_{1,2} < \kappa_{1,2}$) enables microwave to be efficiently trapped in device as coherent photons rather than as rapidly dissipated heat or leaky radiation into far-field . As marked by the red dots in Figs. 2f and h, we define the pure real solution, $\tilde{\omega}_{ZR} \equiv \mathrm{Re}(\tilde{\omega}_{ZR})$ or $\mathrm{Im}(\tilde{\omega}_{ZR}) \equiv 0$, as the perfect zero-reflection (PZR) condition. The PZR frequency can be derived analytically to be,

$$\omega_{PZR} = \frac{1}{2}\frac{sin\,(2\Phi)\,(\omega_1^2-\omega_2^2)}{(\kappa_2-\kappa_1)(cos\,2\,\Phi-1) \pm \left[(\gamma_1+\gamma_2)\,cos\,(2\Phi)+\frac{\kappa_1\gamma_2}{\kappa_2}+\frac{\kappa_2\gamma_1}{\kappa_1}\right]} \qquad (5)$$

The superscript "$\pm$" represents the case that microwave input from port 1 and from port 2, respectively.

The existence of PZR is confirmed experimentally for all three Φ cases ($\Phi = 1.07\pi$, 1.25π and 1.37π), as shown in Figs. 3a-c. For clarity, measurement frequency ω has been shifted by ω_2, i.e., $\Delta_2 \equiv \omega - \omega_2$. Yellow sharp S_{11} reflection dips are clearly visible in Figs. 3a-c (see also Fig. 3d for an enlarged view, marked by black arrow). To reassure the generality, S_{22} spectra have also been measured as shown in Figs. 3g-i where sharp reflection dips show up again (despite that the quantitative Δ_H values for PZR are different due to the asymmetric parameters for two YIG spheres, i.e., $\kappa_1 \neq \kappa_2$). In the above PZR condition, not only reflection vanishes ($|S_{11}(\omega)| = 0$ or $|S_{22}(\omega)| = 0$), but also the spectral linewidth becomes infinitely narrow and effective Q-value becomes ultra-high. As can be seen in Figs. 3f and l, black circles plot the experimental PZR spectra as a function of Δ_2 and gray lines show the calculated results from Eq. (3) with $\Phi = 1.07\pi$. In Fig. 3f, $|S_{11}(\omega)|$ shows an ultra-sharp dip (~67 dB) at $\Delta_H^+/2\pi =$ 9.9 MHz, and, in Fig. 3l, $|S_{22}(\omega)|$ dip appear at $\Delta_H^-/2\pi = -11.0$ MHz, both agreeing well with the theoretical prediction from Eq. (5). An additional intriguing feature of PZR can be revealed

from group delay $\tau_g = -\partial P_{11(22)}/\partial\omega$, which is defined as the negative derivative of the reflection phase $P_{11(22)}$. Fig. 3e (3k) is the group delay τ_g mapping corresponding to Fig. 3d (j). Here, PZR emerges in where the group delay abruptly switches between negative infinity and positive infinity, $\tau_g \to \infty$ at PZR, so that group velocity $v_g = 1/\tau_g$ becomes zero, which reveals that the PZR in our magnonics system is indeed a singularity and can be utilized for slowing microwave photons[26]. For higher Φ values ($\Phi = 1.25\pi$ and 1.37π), PZR is found to take place at $\Delta_H^+/2\pi = 0.9$ MHz (Fig. 3b), $\Delta_H^-/2\pi = -4.1$ MHz (Fig. 3h), and at $\Delta_H^+/2\pi = -2.2$ MHz (Fig. 3c) and $\Delta_H^-/2\pi = -4.8$ MHz (Fig. 3i). All these values agree consistently with the theoretical calculation by Eq. (5).

To understand different role intrinsic ($\gamma_{1,2}$) and external ($\kappa_{1,2}$) dampings are playing, we consider two simplified cases in the following: i) In a symmetrical coupling ($\kappa_1 = \kappa_2$) and lossy condition ($\gamma_{1,2} \neq 0$), Eq. (5) is simplified as $\frac{\omega_1^2-\omega_2^2}{2\omega} = \pm\frac{(\gamma_1+\gamma_2)}{\tan(\omega l/v)}$ (v is the velocity of photon propagation in MTL), which suggests that once the target operating frequency ω_{PZR} is determined, proper distance l values can be decided. In this case, ω_{PZR} still depends on the excitation port and this asymmetry arises from different resonance of two magnonic spheres $\omega_1 \neq \omega_2$. ii) In a lossless system ($\gamma_1 = \gamma_2 = 0$), $\frac{\omega_1^2-\omega_2^2}{2\omega} = 2(\kappa_1 - \kappa_2)\tan(\omega l/v)$, which indicates the PZR is independent of excitation port and can be achieved by adjusting resonant frequencies ($\omega_{1,2}$) and the distance between two resonators (l), as well as the asymmetrical dissipation ($\kappa_{1,2}$) of the system. For generic cases with lossy and asymmetric magnonic resonators as in our experiment, multiple regulation degrees of freedom exist, allowing the PZR condition be generally achievable.

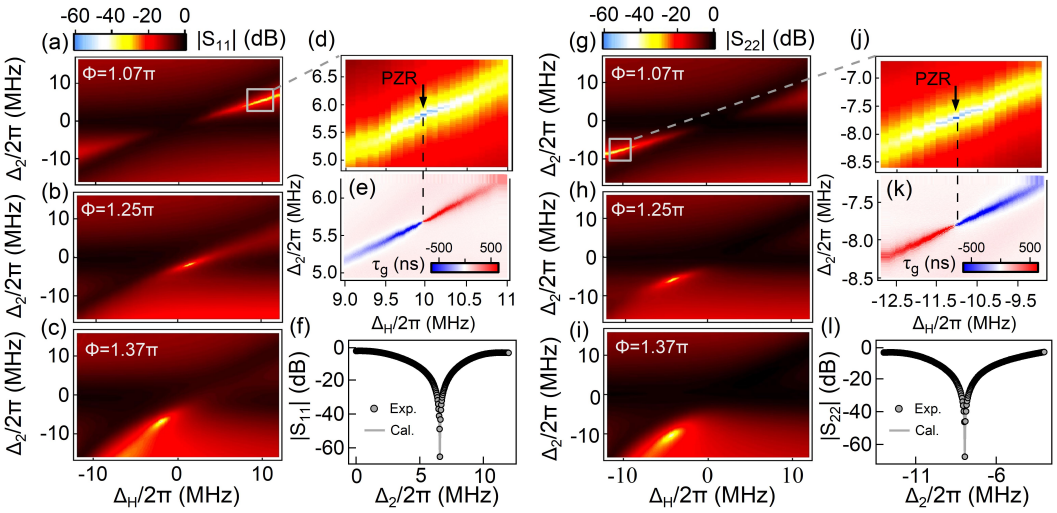

Fig. 3 Perfect zero-reflection condition. a-c Mapping of $|S_{11}|$ as a function of Δ_H and Δ_2 in four cases: fixing $\omega_2/2\pi = 3.6\ GHz, 4.24\ GHz, 4.69\ GHz$. **d** High-resolution zoom-in image of (a). **g-i** Mapping of $|S_{22}|$ as a function of Δ_H and Δ_2 in four ω_2 cases. **j** High-resolution zoom-in image of (g). **e** and **k** are group delay τ_g mappings corresponding to (d) and (j), PZRs emerge as singularities, where the group delay abruptly switches between negative infinity and positive infinity. **f** and **l** are the PZR spectra ($|S_{11}|$ and $|S_{22}|$) at the black arrows marked fields in (d) and (j), respectively.

Transparency and absorption under PZR. Once the PZR condition is satisfied (Eq. (5)), PA and PT can be realized by trading-off the absorption and transmission ($A + T = 1$) and, experimentally, by cooperatively adjusting Φ and Δ_H. On the premise of satisfying Eq. (5), we have numerically analyzed the transmission and absorption from Eq.(4), as shown in Fig. 4a (solid line) and Fig. 4b (dashed line). The transmittivity $t_1 = |S_{21}|^2$ (blue line) and absorptivity $A_1 = 1 - |S_{21}|^2$ (red line) in Fig. 4a show complementary oscillation tendency with Φ. (Gray line represents $r_1 = |S_{11}|^2 = 0$ due to PZR). Fig. 4b shows the data for the case with microwave input from port 2, which show consistent results as Fig. 4a. From Figs. 4a and b, PT can be approached infinitely when Φ gets close to $n\pi/2,\ n \in N^*$, but cannot be reached because $\Phi \neq n\pi/2,\ n \in N^*$, restricted by PZR (Eq. (5)). On the other hand, PA can be approached when Φ gets close to (but still different from) $n\pi/2 + \pi/4$. All experimental datapoints depicted by symbols in Figs. 4a and b show excellent agreement with the numerical results (see Supplementary Note 3 and Fig. S3 for detail measurement data). It is noteworthy pointing out that, as is well-known for two-port

configuration[37], strict PA cannot be reached because PZR ($S_{11}=0$) and ZT ($S_{21}=0$) cannot be satisfied simultaneously (Eqs. (3) and (4)). We emphasize that PZR together with a maximized absorption/minimized transmission is of higher importance from the application point of view, as discussed before. The achievable maxima of absorption under PZR in Fig. 4a reaches ~96% for the input from port 1, and ~80% in Fig. 4b for the input from port 2. This implies that, to realize nearly PA, $\kappa_2 > \kappa_1$ is necessary if microwave is input from port 1 and vice versa. By increasing the ratio of κ_2/κ_1(Supplementary Note 4), the maximum absorption A_1 can be made even closer to ideal unity (while A_2 is sacrificed for the case of input from port 2). In the limit of $\kappa_2/\kappa_1 \to \infty$, the two-port configuration evolves into one-port configuration in which strict PA exists. Experimentally this can be attempted by finely adjusting the distance of YIG spheres to transmission line. Fig. 4c displays a three-dimensional plot of the absorption/transmission when sweeping the YIG 1 resonance ω_1 (and hence Δ_H) and Φ values. while keeping $\omega_2/2\pi = 4.24$ GHz. Nearly PA appears in the small detuning region ($\omega_1 \sim \omega_2$) as indicated by yellow color, and nearly PT takes place in the large detuning region. In the negative detuning region ($\omega_1 < \omega_2$), ω_{PZR} increases with ω_1 at an approximate slope of $\kappa_2/(\kappa_2-\kappa_1)$ and, in the positive detuning region ($\omega_1 > \omega_2$), the slope changes to $\kappa_2/(\kappa_1+\kappa_2)$, this result provide us a guidance to manipulate the microwave propagating and absorption for any target frequency. To sum up, controlling transmission under PZR condition by adjusting H-field (hence retardation phase Φ) and coil current δH-field (hence detuning $\Delta_H \equiv \omega_1 - \omega_2$), our waveguide magnonic device allows the continuous knobbing between nearly PT (infinitely close to 100%) and nearly PA (~96%).

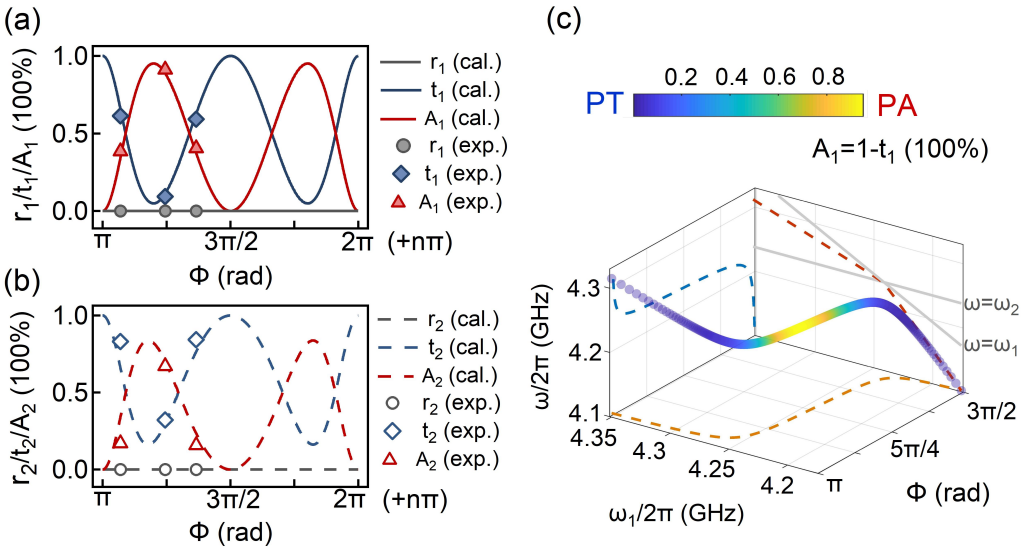

307

308 **Fig. 4 Transition between perfect transparency and nearly perfect absorption. a** For
309 microwave input from port 1, the calculated reflectivity (r_1), transmittivity (t_1) and absorptivity
310 (A_1) as a function of Φ under PZR condition. **b** For microwave input from port 2, the calculated
311 reflectivity (r_2), transmittivity (t_2) and absorptivity (A_2) as a function of Φ under PZR condition.
312 The circle ($r_{1(2)}$), square ($t_{1(2)}$) and triangle ($A_{1(2)}$) symbols in (a) and (b) are the experimental
313 results in different cases of Φ. **c** The three-dimensional plot of the absorption/transmission as a
314 function of Φ, ω_1 and ω. In calculations, $\gamma_1/2\pi = \gamma_2/2\pi = 1$ MHz, $\kappa_1/2\pi = 1.7$ MHz, $\kappa_2/$
315 $2\pi = 3.3$ MHz are set based on the fitting results of experiment spectra.

316

317 ## Conclusion

318 In conclusion, we have demonstrated non-Hermitian control of reflectionless photon propagation,
319 from nearly PT to nearly PA regimes in a magnon-photon coupled system. By freely adjusting the
320 frequency detuning between two magnonic YIG resonators and the retardation phase of travelling
321 microwave photons, the PZR condition can be always achieved with tailored
322 transmission/absorption. The general existence of the reflection singularity in our non-Hermitian
323 magnonic configuration as well as the wide tunability makes the system promising for actual
324 applications. Our work reveals the rich non-Hermitian physics in magnon-photon coupled systems,
325 and meanwhile suggests the broad prospect of non-Hermitian control for practical applications,
326 including microwave circuits, photonic chips, wave optics and future quantum information
327 technologies.

Methods

Device description. The waveguide magnonic device consists of a transmission line and two YIG spheres. The transmission line with width of 1.14 mm and length of 50 mm is fabricated on a 0.762 mm-thick Rogers RO4350B substrate. The dimensions of the substrate is 20×50 mm with a copper thickness of 35 μm on both sides. Two 1 mm diameter YIG spheres separated by 2.5 mm are located on the transmission line. The magnon mode of YIG follows the Kittel dispersion equation $\omega_m = \gamma_e \mu_0 (H + H_0)$, where μ_0 is the vacuum permeability. For YIG 1, the gyromagnetic ratio is $\gamma_e/2\pi = 30\ \mathrm{GHz/T}$, and the anisotropy field is $\mu_0 H_0 = 7.9\ \mathrm{mT}$, as well as for YIG 2, $\gamma_e/2\pi = 29\ \mathrm{GHz/T}$ and $\mu_0 H_0 = 8.4\ \mathrm{mT}$. The static magnetic field is applied perpendicularly to the planar.

Measurement setup. The reflection and transmission spectra are measured using a vector network analyzer (VNA) with an input power of -5 dBm.

References

[1] Rivera, N. & Kaminer, I. Light-matter interactions with photonic quasiparticles. Nat. Rev. Phys. **2**, 538-561 (2020).

[2] Lukin, MD. & Imamoglu, A. Controlling photons using electromagnetically induced transparency. Nature **413**, 273-276 (2001).

[3] Schuller, J A., Barnard, E S., Cai, W. et al. Plasmonics for extreme light concentration and manipulation. Nat. Mater. **9**, 193 (2010).

[4] Xia, F., Mueller, T., Lin, YM., Valdes-Garcia, A. & Avouris, P. Ultrafast graphene photodetector. Nat. Nanotechnol. **4**, 839–843 (2009).

[5] Sukhovatkin, V., Hinds, S., Brzozowski, L. & Sargent, EH. Colloidal Quantum-Dot Photodetectors Exploiting Multiexciton Generation. Science **324**, 1542-1544 (2009).

[6] Peropadre, B., Romero, G., Johansson, G., Wilson, CM. & García-Ripoll, JJ. Perfect Microwave Photodetection in Circuit QED. Phys. Rev. A **84**, 3834 (2010).

[7] Akhlaghi, M K., Schelew, E. & Young, J F. Waveguide Integrated Superconducting Single Photon Detectors Implemented as Coherent Perfect Absorbers. Nat. Commun. **6**, 8233 (2014).

[8] Chuan, F G., Tianyi, S., Feng C., Qian, L. & Ren, Z F. Metallic nanostructures for light

358 trapping in energy-harvesting devices. Light Sci. Appl. **3**, 161 (2014).
359 [9] Ellsworth, D., et al. Photo-spin-voltaic effect. Nat. Phys. **12**, 861-866 (2016).
360 [10] Pantazopoulos, P A., Stefanou, N., Almpanis, E., & Papanikolaou, N. Photomagnonic
361 nanocavities for strong light-spin-wave interaction. Phys. Rev. B **96**, 104425 (2017).
362 [11] Jalas, D. et al. What is- and what is not- an optical isolator. Nat. Photonics. **7**, 579–582
363 (2013).
364 [12] Li Y., Lin J., Guo H., Wu, JS. & Lei, Z. A Tunable Metasurface with Switchable
365 Functionalities: From Perfect Transparency to Perfect Absorption. Adv. Opt. Mater. **8**, 1901548
366 (2020).
367 [13] J, Zhang., Guo, C., Liu, K., Zhu, Z., Ye, W., Yuan, X. & Qin, S. Coherent perfect absorption
368 and transparency in a nanostructured graphene film. Opt. Express **22**, 12524-32 (2014).
369 [14] Yoo, S. & J. Ben. A chip-scale one-way valve for light. Nat. Photonics. **3**, 77-79 (2009).
370 [15] Costas, MS & Martin, Wegener. Past achievements and future challenges in the
371 development of three-dimensional photonic metamaterials. Nat. Photonics. **5**, 523-530 (2011).
372 [16] Papasimakis N., Fedotov, VA., Zheludev, NI. & Prosvirnin, SL. Metamaterial Analog of
373 Electromagnetically Induced Transparency. Phys. Rev. Lett. **101**, 253903 (2008).
374 [17] L, Zhou., W, Wen., Chan, CT. & Ping, S. Electromagnetic-Wave Tunneling Through
375 Negative-Permittivity Media with High Magnetic Fields. Phys. Rev. Lett. **94**, 1-4 (2005).
376 [18] Tassin, P. et al. Electromagnetically Induced Transparency and Absorption in Metamaterials:
377 The Radiating Two-Oscillator Model and Its Experimental Confirmation. Phys. Rev. Lett. **109**,
378 187401 (2012).
379 [19] Mücke, M. et al. Electromagnetically induced transparency with single atoms in a cavity.
380 Nature **465**, 755–758 (2010).
381 [20] Weis, S., Riviere, R., Deleglise, S. et al. Optomechanically Induced Transparency. Science
382 **330**, 1520-1523 (2010).
383 [21] Safavi-Naeini, A H. et al. Electromagnetically induced transparency and slow light with
384 optomechanics. Nature **472**, 69–73 (2011).
385 [22] Regensburger, A. et al. Parity-time synthetic photonic lattices. Nature **488**, 167-171 (2012).
386 [23] Horsley, S., Artoni, M., Rocca, G L. Spatial Kramers–Kronig relations and the reflection of
387 waves. Nat. Photonics. **9**, 436-439 (2015).

[24] Wang, Y P. et al. Nonreciprocity and Unidirectional Invisibility in Cavity Magnonics. Phys. Rev. Lett. **123**, 127202 (2019).

[25] Qian, J., Rao, J W., Gui, Y S., Wang, Y P. & Hu, C M. Manipulation of the zero-damping conditions and unidirectional invisibility in cavity magnonics. Appl. Phys. Lett. **116**, 192401 (2020).

[26] Yang, Y. et al. Unconventional Singularity in Anti-Parity-Time Symmetric Cavity Magnonics. Phys. Rev. Lett. **125**, 147202 (2020).

[27] Changqing, W., Sweeney, W R., Douglas, S A. & Lan, Y. Coherent perfect absorption at an exceptional point. Science **373**, 1261-1265 (2021).

[28] Okuma, N., Kawabata, K., Shiozaki, K. & Sato, M. Topological Origin of Non-Hermitian Skin Effects. Phys. Rev. Lett. **124**, 6801 (2020).

[29] Devoe, R G. & Brewer, R G. Observation of Superradiant and Subradiant Spontaneous Emission of Two Trapped Ions. Phys. Rev. Lett. **76**, 2049 (1996).

[30] Loo, A., Fedorov, A., K, Lalumière. et al. Photon-mediated interactions between distant artificial atoms. **342**, 1494-1496 (2014).

[31] Sato, Y. et al. Strong coupling between distant photonic nanocavities and its dynamic control. Nat. Photonics. **6**, 56-61 (2012).

[32] Friedrich, H., & Wintgen, D. Interfering resonances and bound states in the continuum. Phys. Rev. A **32**, 3231-3242 (1985).

[33] Hsu, C W., Zhen, B., Stone. A D., Joannopoulos, J D. & Soljačić M. Bound states in the continuum. Nat. Rev. Mater. **1**, 16048 (2016).

[34] Zhang, X., Zou, C L., Jiang, L. & Tang, H X. Strongly Coupled Magnons and Cavity Microwave Photons. Phys. Rev. Lett. **113**, 156401 (2014).

[35] Harder, M. et al. Level Attraction Due to Dissipative Magnon-Photon Coupling. Phys. Rev. Lett. **121**, 137203.1-137203.5 (2018).

[36] Pozar, D M. Microwave engineering. John wiley & sons, 2009.

[37] Rao, J W. et al. Interferometric control of magnon-induced nearly perfect absorption in cavity magnonics. Nat. Commun. **12**, 1933 (2021).

Figure legends

Fig. 1 Coherent magnonic system. a Schematic diagram of the experimental setup. Two separated magnons ($l = 25\,mm$) coupled to a transmission line are placed under a vertical magnetic field ($H-$ field), the local magnetic field ($H + \delta H$) around YIG 1 is controllable independently by finely-adjusting coil current. **b** Schematic diagram showing two resonators are side-coupled with a transmission line and interact with each other mediated by travelling wave with the coupling strength of $i\Gamma e^{i\Phi}$. **c** Equivalent circuit of the coupled system. Circuit elements used to model the two YIG spheres are highlighted by the orange and blue box, respectively.

Fig. 2 The evolution between level attraction and level repulsion. a-d blue lines: the frequencies detuning of real parts of eigenvalues $\Delta\mathrm{Re}(\tilde{\omega}_{\pm}) = \mathrm{Re}(\tilde{\omega}_{\pm}) - \omega_2$, orange dashed lines: the frequencies detuning of real part of ZR condition $\Delta\mathrm{Re}(\tilde{\omega}_{ZR}) = \mathrm{Re}(\tilde{\omega}_{ZR}) - \omega_2$ as a function of Δ_H in four Φ cases ($\Phi = n\pi, (n+1/4)\pi, (n+1/2)\pi, (n+3/4)\pi, n \in N^*$). **e-f** Correspondingly, blue lines: the frequencies detuning of the imaginary parts of eigenvalues $\mathrm{Im}(\tilde{\omega}_{\pm})$, orange dashed lines: the imaginary part of ZR condition $\mathrm{Im}(\tilde{\omega}_{ZR})$ as a function of Δ_H. In which blue lines for $\mathrm{Im}(\tilde{\omega}_{\pm})$ correspond to the left *y*-axis and orange dashed lines $\mathrm{Im}(\tilde{\omega}_{ZR})$ correspond to the right *y*-axis.

Fig. 3 Perfect zero-reflection condition. a-c Mapping of $|S_{11}|$ as a function of Δ_H and Δ_2 in four cases: fixing $\omega_2/2\pi = 3.6\,GHz, 4.24\,GHz, 4.69\,GHz$. **d** High-resolution zoom-in image of (a). **g-i** Mapping of $|S_{22}|$ as a function of Δ_H and Δ_2 in four ω_2 cases. **j** High-resolution zoom-in image of (g). **e** and **k** are group delay τ_g mappings corresponding to (d) and (j), PZRs emerge as singularities, where the group delay abruptly switches between negative infinity and positive infinity. **f** and **l** are the PZR spectra ($|S_{11}|$ and $|S_{22}|$) at the black arrows marked fields in (d) and (j), respectively.

Fig. 4 Transition between perfect transparency and nearly perfect absorption. a For microwave input from port 1, the calculated reflectivity (r_1), transmittivity (t_1) and absorptivity (A_1) as a function of Φ under PZR condition. **b** For microwave input from port 2, the calculated reflectivity (r_2), transmittivity (t_2) and absorptivity (A_2) as a function of Φ under PZR condition. The circle ($r_{1(2)}$), square ($t_{1(2)}$) and triangle ($A_{1(2)}$) symbols in (a) and (b) are the experimental

results in different cases of Φ. **c** The three-dimensional plot of the absorption/transmission as a function of Φ, ω_1 and ω. In calculations, $\gamma_1/2\pi = \gamma_2/2\pi = 1$ MHz, $\kappa_1/2\pi = 1.7$ MHz, $\kappa_2/2\pi = 3.3$ MHz are set based on the fitting results of experiment spectra.

Data availability

The data that support the findings of this study are available from the corresponding authors upon reasonable request.

Acknowledgments

This work was funded by NSERC Discovery Grants and NSERC Discovery Accelerator Supplements (C.-M.H.). Z.A acknowledges the financial support from the National Natural Science Foundation of China under Grant Nos. 12027805/11634012/11991060/11674070, the National Key Research Program of China under Grant No. 2016YFA0302000, and the Shanghai Science and Technology Committee under Grant Nos. 18JC1420402, 18JC1410300, 20JC1414700, 20DZ1100604. J. Qian was supported in part by the China Scholarship Council (CSC). We thank Yipu Wang for discussion and providing conceptual advice.

Author Contribution

Y.S.G conceived the idea and designed the experiments. J.W.R prepared the samples and built up the experiment setup. Q.J. performed all the experiments. Q.J., Y.S.G., Z.A. and C.M.Hu performed the data analysis and co-wrote the manuscript with comments from all authors. Z.J.R provides help in data analysis and discussion. C.M.Hu and Z.A. supervised the project.

Competing interests

The authors declare no competing interests.

Supplementary Files

This is a list of supplementary files associated with this preprint. Click to download.

- SupplementaryInformation.pdf